Tetrahedral composite finite elements

P. Thoutireddy, J. F. Molinari, E. A. Repetto and M. Ortiz[*],[†]

Graduate Aeronautical Laboratories, California Institute of Technology, Pasadena, CA 91125, U.S.A.

SUMMARY

We develop and analyse a composite 'CT3D' tetrahedral element consisting of an ensemble of 12 four-node linear tetrahedral elements, coupled to a linear assumed deformation defined over the entire domain of the composite element. The element is designed to have well-defined lumped masses and contact tractions in dynamic contact problems while at the same time, minimizing the number of volume constraints per element. The relation between displacements and deformations is enforced weakly by recourse to the Hu–Washizu principle. The element arrays are formulated in accordance with the 'assumed-strain' prescription. The formulation of the element accounts for fully non-linear kinematics. Integrals over the domain of the element are computed by a five-point quadrature rule. The element passes the patch test in arbitrarily distorted configurations. Our numerical tests demonstrate that CT element has been found to possess a convergence rate comparable to those of linear simplicial elements, and that these convergence rates are maintained as the near-incompressible limit is approached. We have also verified that the element satisfies the Babuška–Brezzi condition for a regular mesh configuration. These tests suggest that the CT3D element can indeed be used reliably in calculations involving near-incompressible behaviour which arises, e.g., in the presence of unconfined plastic flow. Copyright © 2001 John Wiley & Sons, Ltd.

KEY WORDS: finite element analysis; composite element; contact; dynamics; inf–sup test

1. INTRODUCTION

Camacho and Ortiz [1, 2] briefly described the triangular and tetrahedral elements constructed by assembling linear subtriangles and tetrahedra and coupling them to a continuous linear strain field over the assemblage. They called these elements *composite* triangular and tetrahedral, or CT, elements. The advantages of these elements arise primarily in explicit time integration and contact-impact problems, where the lumped mass of their midside nodes is well matched to their corner node masses. This feature effectively overcomes the difficulties inherent to quadratic simplicial elements, for which the row-sum method of lumping results in zero or negative corner masses. Furthermore, the volumetric locking which characterizes

---

linear simplicial elements is eliminated. Thus, the composite elements appear to combine the best attributes of linear and quadratic simplicial elements, including the ease of mesh generation, without their drawbacks.

Guo *et al.* [3] have presented a detailed analysis of several composite triangular elements and have established their basic behaviour. This study has shown that the CT elements have a rate of convergence in energy norm which is comparable to the six-node element for compressible materials though the rate of convergence in the displacements is of the same order as the linear-displacement three-node triangle. The elements pass the patch test in arbitrarily distorted configurations. For incompressible problems, the performance of the linear strain element is not as satisfactory. Guo *et al.* [3] proposed an alternative composite triangle in which the volumetric strain is assumed to be constant over the assemblage and showed that this element satisfies the Babuška–Brezzi criterion.

In this paper, we propose and analyse a composite tetrahedral element. The proposed ten-node CT element is a composite of 12 four-node tetrahedral elements with a linear displacement field in each one of them. The relation between displacements and deformations is enforced weakly by recourse to the Hu–Washizu principle (References e.g. [1–4]). The formulation of the element allows for fully non-linear kinematics. We verify that the element passes the patch test in arbitrarily distorted configurations. In addition, for compressible materials the CT element is found to possess a convergence rate in the energy and pressure norms which is comparable to linear elements. Finally, we verify that the element passes the Babuška–Brezzi criterion and performs well in the near-incompressible limit.

2. MODEL PROBLEM

We consider a solid occupying a region $B_0 \in \mathbb{R}^3$ in its reference undeformed configuration. The solid subsequently deforms under the action of externally applied forces and prescribed displacements. The deformation mapping $\boldsymbol{\varphi} : B_0 \to \mathbb{R}^3$ maps material points $\mathbf{X}$ in the reference configuration into their corresponding positions $\mathbf{x}$ in the deformed configuration $B = \boldsymbol{\varphi}(B_0)$. The deformation gradient field follows as $\mathbf{F} = \nabla_0 \boldsymbol{\varphi}$, where ∇_0 is the material gradient. In components

$$F_{iJ} = \frac{\partial \varphi_i}{\partial X_J} \quad \text{in } B_0 \tag{1}$$

Here and subsequently, we use upper (respectively, lower) case indices to denote components of vector fields defined over the undeformed (respectively, deformed) configuration. The deformation mapping is prescribed to take a prescribed value $\bar{\boldsymbol{\varphi}}$ over the displacement part ∂B_{01} of the undeformed boundary. This furnishes the boundary condition

$$\varphi_i = \bar{\varphi}_i \quad \text{on } \partial B_{01} \tag{2}$$

Additionally, the solid is in equilibrium, which requires

$$P_{iJ,J} + \rho_0 B_i = 0 \quad \text{in } B_0 \tag{3}$$

and

$$P_{iJ}N_J = \bar{T}_i \quad \text{on } \partial B_{02} \tag{4}$$

Here, $\mathbf{P}$ denotes the first Piola–Kirchhoff stress tensor, ρ_0 is the mass density per unit unde-formed volume, $\mathbf{B}$ is the body force density per unit mass, $\mathbf{N}$ is the unit normal to the unde-formed boundary, and $\bar{\mathbf{T}}$ is the applied traction over the traction boundary $\partial B_{02} = \partial B_0 - \partial B_{01}$. For simplicity, we shall assume that the material is elastic, with strain-energy density $W(\mathbf{F})$. Under these assumptions, the constitutive relations take the form

$$P_{iJ} = \frac{\partial W}{\partial F_{iJ}}(\mathbf{F}) \equiv P_{iJ}(\mathbf{F}) \tag{5}$$

With a view to formulating finite-element approximations, we begin by restating the preced-ing equations in variational form. The conventional displacement finite-element method may be regarded as the result of effecting a constrained minimization of the potential energy

$$\mathbf{\Phi} = \int_{B_0} [W(\nabla_0 \mathbf{\varphi}) - \rho_0 B_i \varphi_i] \, \mathrm{d}V_0 - \int_{\partial B_{02}} \bar{T}_i \varphi_i \, \mathrm{d}S_0 \tag{6}$$

among all finite-element deformation mappings. More general finite-element methods may be derived from the Hu-Washizu principle. The Hu-Washizu potential of the solid is

$$I[\mathbf{\varphi}, \mathbf{F}, \mathbf{P}] = \int_{B_0} [W(\mathbf{F}) + P_{iJ}(\varphi_{i,J} - F_{iJ}) - \rho_0 B_i \varphi_i] \, \mathbf{d}V_0$$

$$- \int_{\partial B_{01}} P_{iJ} N_J (\varphi_i - \bar{\varphi}_i) \, \mathrm{d}S_0 - \int_{\partial B_{02}} \bar{T}_i \varphi_i \, \mathrm{d}S_0 \tag{7}$$

The stationarity of I demands

$$\int_{B_0} (P_{iJ} \delta\varphi_{i,J} - \rho_0 B_i \delta\varphi_i) \, \mathrm{d}V_0 - \int_{\partial B_{01}} P_{iJ} N_J \delta\varphi_i \, \mathrm{d}S_0 - \int_{\partial B_{02}} \bar{T}_i \delta\varphi_i \, \mathrm{d}S_0 = 0 \tag{8}$$

$$\int_{B_0} [W,_{F_{iJ}}(\mathbf{F}) - P_{iJ}] \delta F_{iJ} \, \mathrm{d}V_0 = 0 \tag{9}$$

$$\int_{B_0} (\varphi_{i,J} - F_{iJ}) \delta P_{iJ} \, \mathrm{d}V_0 - \int_{\partial B_{01}} \delta P_{iJ} N_J (\varphi_i - \bar{\varphi}_i) \, \mathrm{d}S_0 = 0 \tag{10}$$

which is a weak restatement of the field equations and boundary conditions of the prob-lem. The appeal of the Hu–Washizu principle in the present context is that it allows for the independent interpolation of displacements, deformations and stresses. The use of the Hu–Washizu principle to formulate mixed elements was pioneered by Simó [5].

3. ELEMENT DESCRIPTION

The proposed element consists of 12 four-node sub-elements, each of which is equipped with linear displacement interpolation. This piecewise linear displacement interpolation scheme is coupled to linear assumed deformation and stress fields defined over the entire domain of
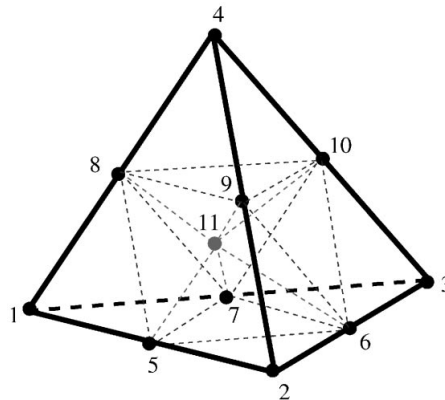
Figure 1. The geometry and nodal numbering convention of the CT3D composite element.

the element. One motivation for this choice of interpolation is to obtain an element in which lumped nodal masses are unambiguously and appropriately defined and are well matched to contact tractions in impact problems. This is accomplished by interpolating displacements in a piecewise linear fashion. The choice of deformation and stress interpolation is designed so as to introduce four volume constraints per element in the near-incompressible limit.

The geometry and nodal numbering convention of the element are depicted in Figure 1. It should be carefully noted that the element edges need not be straight, i.e. the centre node of the edges need not be at the midpoint of the segment defined by the corresponding vertices. We additionally introduce an auxiliary node at position

$$\mathbf{X}_{11} = \frac{1}{6} \sum_{a=5}^{10} \mathbf{X}_a \tag{11}$$

where $\mathbf{X}_a$, $a = 1, \ldots, 10$ are the undeformed nodal coordinates. Likewise, the position of the auxiliary node in the deformed configuration is constrained to be

$$\mathbf{x}_{11} = \frac{1}{6} \sum_{a=5}^{10} \mathbf{x}_a \tag{12}$$

in accordance with the assumed linear interpolation. The introduction of an auxiliary 11th node such as described ensures that, in its regular tetrahedral configuration, the element possesses all the expected symmetries. In particular, all the mid-edge nodes are given the same weight. The 12 sub-elements are defined by the connectivity array in Table I.

The interpolation scheme just described defines a set of piecewise linear shape functions $\{N_a, \ a = 1, \ldots, 10\}$ defined over the undeformed domain of the element. In particular, the interpolated deformation mapping is

$$\boldsymbol{\varphi}(\mathbf{X}) = \sum_{a=1}^{10} \mathbf{x}_a \mathbf{N}_a(\mathbf{X}) \tag{13}$$

where $\{\mathbf{x}_a, \ a = 1, \ldots, 10\}$ are deformed nodal coordinates.

Table I. Connectivity array for the 12 sub-elements of the CT3D composite element.

Tetrahedron	Node 1	Node 2	Node 3	Node 4
1	1	5	7	8
2	2	6	5	9
3	3	7	6	10
4	4	9	8	10
5	5	9	6	11
6	6	9	10	11
7	10	9	8	11
8	8	9	5	11
9	5	6	7	11
10	6	10	7	11
11	10	8	7	11
12	8	5	7	11

Independent of the displacement interpolation just described, we adopt an 'assumed' linear representation of the deformation and stress fields of the form

$$\bar{\mathbf{F}}(\mathbf{X}) = \sum_{a=1}^{4} \mathbf{F}_a \lambda_a(\mathbf{X}) \tag{14}$$

$$\bar{\mathbf{P}}(\mathbf{X}) = \sum_{a=1}^{4} \mathbf{P}_a \lambda_a(\mathbf{X}) \tag{15}$$

where $\{\lambda_a, \; a = 1, \ldots, 4\}$ are the barycentric coordinates associated with the four vertices of the parent element and $\{\mathbf{F}_a, \; a = 1, \ldots, 4\}$ and $\{\mathbf{P}_a, \; a = 1, \ldots, 4\}$ are matrices of coefficients. Evidently, the assumed deformations are not the gradients of the interpolated deformation mapping (13) in general. Likewise, the assumed stress field does not follow from an application of the constitutive relations to the gradients of the interpolated mapping. Instead, we enforce these relations weakly in the sense of Equations (8)–(10). In particular, from Equation (10) we obtain the system of equations:

$$\sum_{b=1}^{4} \left\{ \int_{\Omega_0} \lambda_a \lambda_b \, \mathrm{d}V_0 \right\} F_{iJb} = \sum_{b=1}^{10} \left\{ \int_{\Omega_0} \lambda_a N_{b,J} \, \mathrm{d}V_0 \right\} x_{ib} \tag{16}$$

where Ω_0 is the undeformed domain of the element and we have assumed that the displacement boundary conditions are identically satisfied by the displacement interpolation. Solving (16) for the coefficients $\mathbf{F}_a$ and inserting the result into (14) yields the relation

$$\bar{F}_{iJ}(\mathbf{X}) = \sum_{a=1}^{10} x_{ia} \bar{L}_{aJ}(\mathbf{X}) \tag{17}$$

where

$$\bar{L}_{aJ}(\mathbf{X}) = \sum_{b=1}^{4} \sum_{c=1}^{4} \lambda_c(\mathbf{X}) M_{cb}^{-1} \int_{\Omega_0} \lambda_b N_{a,J} \, \mathrm{d}V_0 \tag{18}$$

and we write

$$M_{bc} = \int_{\Omega_0} \lambda_b \lambda_c \, dV_0 \tag{19}$$

Equation (17) gives the assumed deformation field in terms of the deformed nodal coordinates and replaces the conventional relation

$$\mathbf{F}_{iJ}(\mathbf{X}) = \sum_{a=1}^{10} x_{ia} N_{a,J}(\mathbf{X}) \equiv \sum_{a=1}^{10} x_{ia} L_{aJ}(\mathbf{X}) \tag{20}$$

of the displacement finite-element method. We also note that the matrix inversion in (18) needs to be carried out only once in the course of a calculation.

Taking variations in (17) gives the relation

$$\delta \bar{F}_{iJ}(\mathbf{X}) = \sum_{a=1}^{10} \delta x_{ia} \bar{L}_{aJ}(\mathbf{X}) \tag{21}$$

which upon substitution into (8) yields the internal and external force arrays

$$f_{ia}^{\text{int}} = \int_{\Omega_0} \bar{P}_{iJ} \bar{L}_{aJ} \, dV_0 \tag{22}$$

$$f_{ia}^{\text{ext}} = \int_{\Omega_0} \rho_0 B_i N_a \, dV_0 + \int_{\partial \Omega_{02}} \bar{T}_i N_a \, dS_0 \tag{23}$$

In arriving at these expressions we have restricted $\delta \boldsymbol{\varphi}$ to satisfy homogeneous essential boundary conditions, i.e. we have required that $\delta \varphi_i = 0$ on ∂B_{01}. We also note that in (23) $\partial \Omega_{02}$ denotes $\partial \Omega_0 \cap \partial B_{02}$, i.e. it is the part of the boundary of the element, possibly empty, which lies on the traction boundary.

Finally, we turn to the weak form (9) of the constitutive relations. Inserting (14) and (15) into (9) and solving the resulting system of linear equations gives

$$P_{iJb} = \sum_{a=1}^{4} M_{ba}^{-1} \int_{B_0} P_{iJ}(\bar{\mathbf{F}}) \lambda_a \, dV_0 \tag{24}$$

and the stress field follows in the form

$$\bar{P}_{iJ} = \sum_{a=1}^{4} \sum_{b=1}^{4} \lambda_b(\mathbf{X}) M_{ba}^{-1} \int_{B_0} P_{iJ}(\bar{\mathbf{F}}) \lambda_a \, dV_0 \tag{25}$$

This field may now be used in (22) to compute the internal force array.

In the calculations, we evaluate the integrals in (19) and (22) by the five-point Gaussian quadrature rule (as when compared to a four-point quadrature scheme required for the usual isoparametric element) defined in Table II. In this table, V_i denotes the volume of sub-element i. In principle, the integral in the stress-reduction formula (25) could be computed by the same means. However, this would render the computation of the stresses somewhat costly. Instead,

Table II. Five-point quadrature rule.

λ_1	λ_2	λ_3	λ_4	Quadrature weight
1/4	1/4	1/4	1/4	$(V_5 + V_7 + V_{10} + V_{12})/2 + V_6 + V_8 + V_9 + V_{11}$
1/2	1/6	1/6	1/6	$V_1 + V_{12}/2$
1/6	1/2	1/6	1/6	$V_2 + V_5/2$
1/6	1/6	1/2	1/6	$V_3 + V_{10}/2$
1/6	1/6	1/6	1/2	$V_4 + V_7/2$
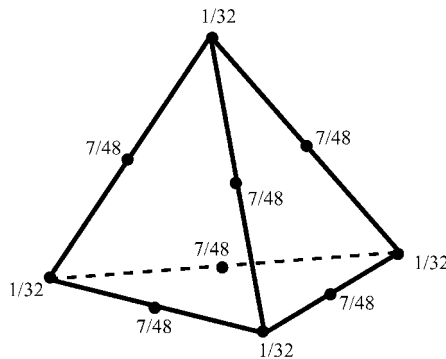
Figure 2. Lumped-mass distribution for the CT3D composite element.

we choose to satisfy the constitutive relations by simply evaluating (5) pointwise using the assumed deformation field (17). The resulting internal forces are

$$f_{ia}^{\text{int}} = \int_{\Omega_0} P_{iJ}(\bar{\mathbf{F}})\bar{L}_{aJ}\,\mathrm{d}V_0 \tag{26}$$

This expression may be obtained directly by rendering stationary the 'assumed' potential energy

$$\mathbf{\Phi} = \int_{B_0} [W(\bar{\mathbf{F}}) - \rho_0 B_i \varphi_i]\,\mathrm{d}V_0 - \int_{\partial B_{02}} \bar{T}_i \varphi_i \,\mathrm{d}S_0 \tag{27}$$

Note that, in this expression, the strain energy is evaluated from the assumed deformation field directly. This implementation is in the spirit of Hughes's $\bar{\mathbf{B}}$ method for anisotropic linear elasticity [6], in which the discrete strain operator, or $\mathbf{B}$ matrix, is replaced by an assumed matrix $\bar{\mathbf{B}}$ in the strain energy density. The resulting finite-element method may be obtained from the standard displacement finite-element method by formally replacing the material shape-function gradients $N_{a,J}$ by the the array $\bar{L}_{aJ}$ defined in (18). This substitution may conveniently be made at the shape-function routine level, and the remaining structure of the element routine is identical to that of the displacement finite-element method.

We also note that a lumped-mass matrix for the composite element may be simply computed by assembling the standard lumped-mass matrices of the twelve four-node sub-elements. The resulting nodal mass distribution is depicted in Figure 2. As is evident from this

figure, all nodal masses are strictly positive. This is in contrast to the lumped masses for the quadratic 10-node element obtained by the row-sum method, which are negative at the corner nodes.

4. NUMERICAL TESTS

In this section, we report the results of a number of standard tests which establish the accuracy, stability and convergence characteristics of the CT3D composite element. As a first elementary test, we have verified that the element passes the patch test in arbitrary distorted configurations, and that the tangent stiffness matrices are not rank-deficient and, therefore, are devoid of spurious zero-energy modes. It should be noted that, for the patch test to be satisfied for arbitrary element geometries, care must be exercised to employ the same quadrature scheme in the calculations of the assumed shape-function gradients and the element force and stiffness arrays. We have also assessed the convergence characteristics of the element in selected linear benchmark cases, and demonstrated the stability of the element in the near-incompressible limit with the aid of the inf–sup test of Babuška and Brezzi [7, 8]. These tests are subsequently discussed in turn.

4.1. Convergence tests

We have performed two standard benchmark tests: the bending of a linear-elastic cantilever strip under the action of a tip load; and the stretching of a linear-elastic infinite plate with a circular hole. In order to test the three-dimensional composite element, we solve these problems in three dimensions. The following norms and seminorms are used to quantify solution errors and gauge the performance of the element:

$$\|\mathbf{u}\|_0 = \left\{ \int_\Omega |\mathbf{u}|^2 \, d\Omega \right\}^{1/2} \tag{28}$$

$$|\mathbf{u}|_E = \left\{ \int_\Omega \sigma_{ij} u_{i,j} \, d\Omega \right\}^{1/2} \tag{29}$$

$$\|p\|_0 = \left\{ \int_\Omega p^2 \, d\Omega \right\}^{1/2} \tag{30}$$

where $\mathbf{u}$, $\boldsymbol{\sigma}$ and p are the displacement, stress and pressure fields, respectively. Evidently, $\|\mathbf{u}\|_0$ and $\|p\|_0$ are the L_2 norms of $\mathbf{u}$ and p, respectively, whereas $|\mathbf{u}|_E$ is the energy seminorm of $\mathbf{u}$. In the calculations, all norms are computed by the five-point numerical quadrature rule described in the foregoing.

4.1.1. Cantilever strip problem. Next, we consider the problem of a linear-elastic infinite cantilever strip under the action of a tip load P per unit length, Figure 3. The strip has a uniform thickness t and length L. A system of orthonormal cartesian axes is chosen such that x_1 runs the width of the strip and x_3 points in its normal direction along the thickness. Provided that the tip load is distributed appropriately over the end section of the strip, the
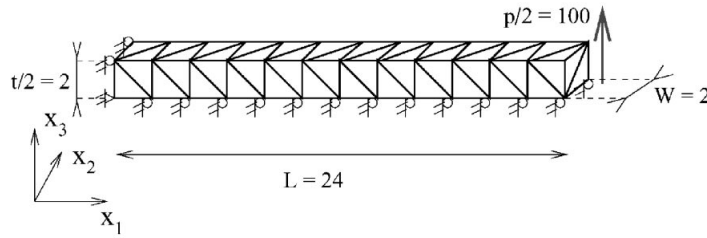
Figure 3. Sample mesh for the cantilever strip test problem showing the mesh design used in the calculations.

solution to this problem is elementary (e.g. Reference [9]), and is given by

$$u_1 = \frac{-Px_3}{6D}\{(6L - 3x_1)x_1 + (2 + \bar{v})[x_3^2 - (t/2)^2]\} \tag{31}$$

$$u_2 = 0 \tag{32}$$

$$u_3 = \frac{P}{6D}[3\bar{v}x_3^2(L - x_1) + (4 + 5\bar{v})(t/2)^2x_1 + (3L - x_1)x_1^2] \tag{33}$$

and

$$\sigma_{11} = -\frac{12Px_3}{t^3}(L - x_1) \tag{34}$$

$$\sigma_{22} = -\frac{12vPx_3}{t^3}(L - x_1) \tag{35}$$

$$\sigma_{13} = -\frac{6P}{t^3}[2(t/2)^2 - x_3^2] \tag{36}$$

$$\sigma_{33} = \sigma_{12} = \sigma_{23} = 0 \tag{37}$$

Here

$$D = \frac{Et^3}{12(1 - v^2)} \tag{38}$$

$$\bar{v} = v/(1 - v) \tag{39}$$

E and v are the Young's modulus and Poisson's ratio of the material, respectively, and D is the bending stiffness of the plate.

Owing to the anti-symmetry of the problem about the neutral fibre of the plate, only the upper half of the plate is discretized. The analysis is carried out in three dimensions by discretizing a finite width W of the strip and subjecting the lateral surfaces $x_2 = 0$ and $x_2 = W$ to the boundary condition $u_2 = 0$. The section $x_1 = 0$ of the strip is built in. Nodal forces computed from (36) are computed over the end section $x_1 = L$. The numerical values of the parameters
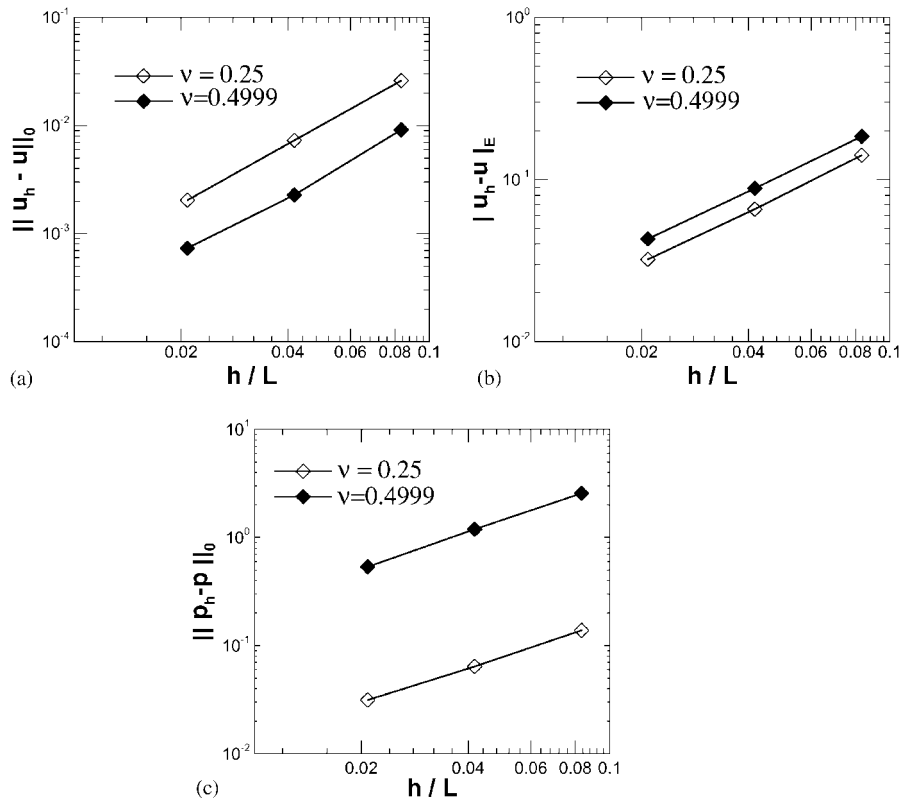
Figure 4. Convergence plots for the cantilever strip test problem: (a) L_2-norm of displacement error; (b) energy norm of displacement error; (c) L_2-norm of pressure error.

Table III. Convergence rates for the cantilever strip test problem.

v	$\|\mathbf{u}_h - \mathbf{u}\|_0$	$|\mathbf{u}_h - \mathbf{u}|_E$	$\|p_h - p\|_0$
0.2500	1.8375	1.0669	1.0706
0.4999	1.8203	1.0500	1.1289

used in the calculations are: $L = 24$, $W = 2$, $t = 4$, $P = 200$, $E = 3 \times 10^7$, and $v = 0.25, 0.4999$. The latter value of the Poisson's ratio renders the material nearly incompressible. The domain of analysis is partitioned into cubic blocks, and these blocks are subsequently discretized into tetrahedral elements as shown in Figure 3.

Figure 4 shows the dependence of various normalized error norms on mesh size (h). The error norms are normalized by the corresponding norm of the exact field. The convergence rates deduced from these plots are collected in Table III. The convergence rate is the slope of the error vs mesh-size curve in the logarithmic axes. The theoretical rates of convergence
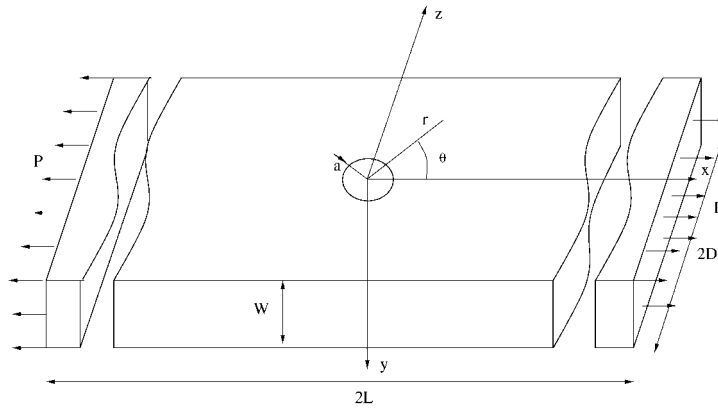
Figure 5. Infinite plate with a circular hole.

of the errors $\|\mathbf{u}_h - \mathbf{u}\|_0$, $|\mathbf{u}_h - \mathbf{u}|_E$ and $\|p_h - p\|_0$ for simplicial tetrahedra are $k + 1$, k and k, respectively, where k is the order of interpolation. As may be seen from Table III, the computed rates in the L_2 norm of the displacement field is slightly below the theoretical value of linear interpolation, $k = 1$. By contrast, the convergence rates in pressure and the energy norm are slightly better than those for linear interpolation. It is evident from the convergence plots that the accuracy of the element degrades somewhat in the near-incompressible limit. However, it is interesting to note that the convergence rates are maintained in that limit.

4.1.2. Infinite plate with a circular hole problem. We consider an infinite plate containing a circular hole of radius *a* deforming in plane strain under the action of a remotely applied uniaxial tension σ, Figure 5. We refer the plate of analysis to a system of polar coordinates (r, θ) and we denote the perpendicular coordinate by *y*. The analytical solution to this problem is (e.g. Reference [9])

$$u_r = \frac{p(1+v)}{2E}\left[\frac{1-\bar{v}}{1+\bar{v}}r + \frac{a^2}{r} + \left(r - \frac{a^4}{r^3} + \frac{4a^2}{(1+\bar{v})r}\right)\cos 2\theta\right] \tag{40}$$

$$u_\theta = -\frac{p(1+v)}{2E}\left(r + \frac{a^4}{r^3} + \frac{1-\bar{v}}{1+\bar{v}}\frac{2a^2}{r}\right)\sin 2\theta \tag{41}$$

and

$$\sigma_{rr} = \frac{p}{2}\left[\left(1 - \frac{a^2}{r^2}\right) + \left(1 + \frac{3a^4}{r^4} - \frac{4a^2}{r^2}\right)\cos 2\theta\right] \tag{42}$$

$$\sigma_{\theta\theta} = \frac{p}{2}\left[\left(1 + \frac{a^2}{r^2}\right) - \left(1 + \frac{3a^4}{r^4}\right)\cos 2\theta\right] \tag{43}$$

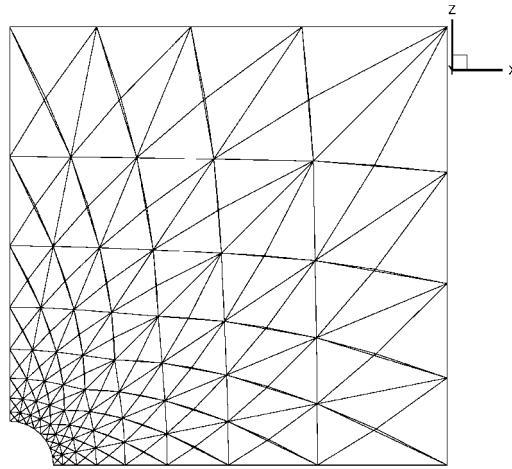Figure 6. Sample mesh used in the plate with a circular hole test problem.

$$\sigma_{yy} = vp \left(1 - \frac{2a^2}{r^2} \cos 2\theta \right) \tag{44}$$

$$\sigma_{r\theta} = -\frac{p}{2} \left(1 - \frac{3a^4}{r^4} + \frac{2a^2}{r^2} \right) \sin 2\theta \tag{45}$$

$$\sigma_{ry} = \sigma_{\theta y} = 0 \tag{46}$$

Owing to the symmetries of the problem, the domain of analysis may be restricted to one quadrant of the (r, θ) plane. We carry out the calculations in three dimensions by discretizing a slab of material of thickness W. We additionally restrict the analysis to a finite square region in the (r, θ) plane of size $10a$. The exact analytical displacements (40) and (41) are prescribed on the remote edges of the domain of analysis. The numerical values of the parameters used in the calculations are: $a = 0.1$, $W = 0.1$, $\sigma = 200$, $E = 3 \times 10^7$, and $v = 0.25, 0.4999$. As in the cantilever strip problem, this latter value of the Poisson's ratio tests the performance of the element in the near-incompressible range. A typical mesh used in the calculations is shown in Figure 6.

Figure 7 shows the dependence of various normalized error norms on mesh size(h). The error norms are normalized by the corresponding norm of the exact field. The convergence rates deduced from these plots are collected in Table IV. As may be seen from this table, all the convergence rates are slightly better than those corresponding to linear simplicial elements, except for the pressure error in the near-incompressible case, which lags somewhat behind the theoretical convergence rate. In general, the computed errors are larger in the near-incompressible case, which suggests a certain loss of accuracy of the element in that limit. However, despite this absolute accuracy loss, the rates of convergence appear to be maintained as the incompressible limit is approached.
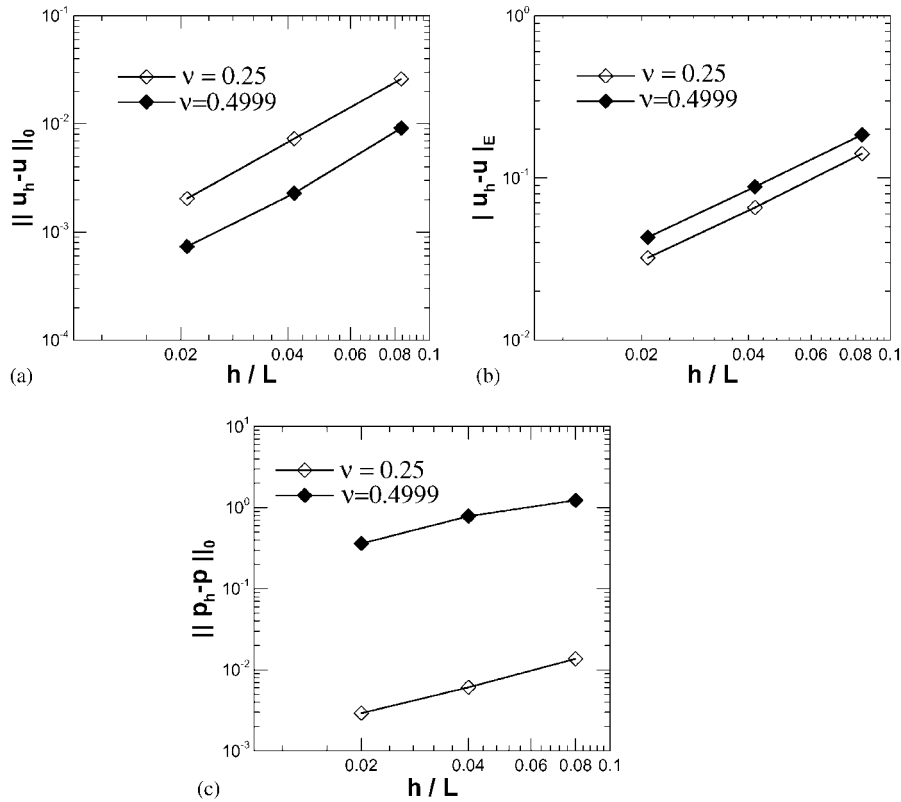
Figure 7. Convergence plots for the plate with a circular hole test problem: (a) L_2-norm of displacement error; (b) energy norm of displacement error; (c) L_2-norm of pressure error.

Table IV. Convergence rates for the plate with a circular hole test problem.

v	$\|\mathbf{u}_h - \mathbf{u}\|_0$	$\|\mathbf{u}_h - \mathbf{u}\|_E$	$\|p_h - p\|_0$
0.2500	2.0511	1.0255	1.1145
0.4999	2.0148	1.0316	0.8848

4.2. Inf–sup test

Our final test is aimed at establishing whether the Babuška–Brezzi [7, 8] stability condition is satisfied by the composite CT3D element in the incompressible limit. The satisfaction of the Babuška–Brezzi condition guarantees the convergence of finite-element schemes in the near-incompressible regime and, thus, establishes the absence of volumetric locking. Unfortunately, a rigorous verification of the Babuška–Brezzi condition for specific classes of elements and arbitrary meshes is difficult. Here, instead, we follow a procedure proposed by Chapelle and
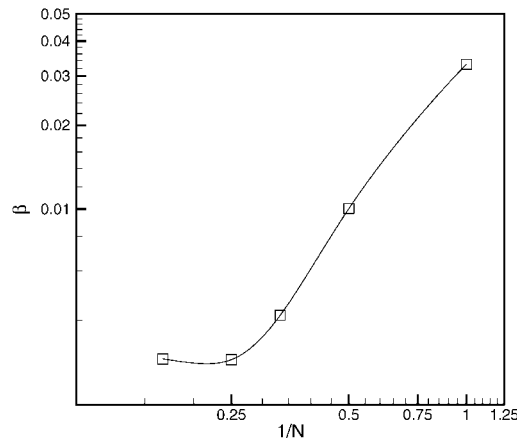
Figure 8. Asymptotic plot of the inf–sup value for the composite element.

Bathe [10] (see also Reference [11]) which is based on evaluation of specific meshes and, therefore, furnishes a test—if not a definitive proof—of stability.

In Chapelle and Bathe inf–sup test, an upper bound β_h to the stability parameter is obtained as the square root of the minimum non-zero eigenvalue of the generalized symmetric eigenvalue problem

$$\mathbf{G}_h\mathbf{v}_h = \lambda_h\mathbf{S}_h\mathbf{v}_h \tag{47}$$

where $\mathbf{S}_h$ is the positive-definite symmetric matrix which delivers the L_2 norm $\|\mathbf{u}_h\|_0$, and $\mathbf{G}_h$ is the positive semi-definite symmetric matrix which delivers the seminorm $\int_\Omega p_h\nabla\cdot\mathbf{u}_h\mathrm{d}\Omega$. The procedure consists of computing the stability parameter β_h and verifying that it remains bounded below as the element size $h\to 0$.

We specifically consider a linear-elastic cubic block of Poisson's ratio $v = 0.4999$. In order to mesh the domain of analysis, partition it into cubes and subsequently discretize each cube into 12 composite elements. A sequence of meshes is generated by regular refinement and the stability parameter β_h is computed for each element size h. The result of the calculations is shown in Figure 8. This figure suggests that β_h indeed remains bounded below as $h\to 0$ for the specific sequence of meshes under consideration. This asymptotic behaviour of β_h suggests that the composite CT3D element is indeed free of volumetric locking.

5. SUMMARY AND CONCLUSIONS

We have developed and analysed a composite 'CT3D' tetrahedral element consisting of 12 four-node linear tetrahedral elements and a linear assumed deformation defined over the entire domain of the composite element. The element is designed to have well-defined lumped masses and contact tractions in dynamic contact problems, which is accomplished by endowing the element with a piecewise-linear displacement interpolation, while at the same time minimizing the number of volume constraints per element, which is accomplished by

equipping the element with linear assumed deformations. The relation between displacements and deformations is enforced weakly by recourse to the Hu–Washizu principle. The element arrays are formulated in accordance with the 'assumed-strain' prescription. However, our formulation of the element accounts for fully non-linear kinematics. Integrals over the domain of the element are computed by a five-point quadrature rule.

We have verified that the element passes the patch test in arbitrarily distorted configurations. In addition, for compressible and near-incompressible materials, the CT element has been found to possess a convergence rate comparable to those of linear simplicial elements. We have also verified that the element satisfies the Babuška–Brezzi condition as shown by Chapelle and Bathe [10, 11]. These tests suggest that the CT3D element can indeed be used reliably in calculations involving near-incompressible behaviour which arises, e.g. in the presence of unconfined plastic flow.

REFERENCES

1. Camacho GT, Ortiz M. Computational modeling of impact damage in brittle materials. *International Journal of Solids and Structures* 1996; **33**:2899–2938.
2. Camacho GT. Computational modelling of impact damage and penetration of brittle and ductile materials. Ph.D. Dissertation, Brown University, Providence, RI, 1995.
3. Guo Y, Ortiz M, Belytschko T, Repetto EA. Triangular composite finite elements. *International Journal for Numerical Methods in Engineering* 2000; **47**:287–316.
4. Zienkiewicz OC, Liu YC, Huang GC. Error estimates and convergence rates for various compressible materials. *International Journal for Numerical Methods in Engineering* 1989; **28**:2191–2202.
5. Simo JC, Hughes TJR. On the variational foundation of the assumed strain methods. *Journal of Applied Mechanics* 1986; **53**:51–54.
6. Hughes TJR. Generalization of selective integration procedures to anisotropic and nonlinear media. *International Journal for Numerical Methods in Engineering* 1980; **15**:1413–1418.
7. Babuška I. Error bounds for finite element method. *Numerische Mathematik* 1971; **16**:322–333.
8. Brezzi F. On the existence, uniqueness and approximation of saddle-point problems arising from Lagrange multipliers. *RAIRO, 1974*; **8**:129–151.
9. Timoshenko SP, Goodier JN. *Theory of Elasticity* (3rd edn). McGraw-Hill: New York, 1970.
10. Chappelle D, Bathe KJ. The inf–sup test. *Computers and Structures* 1993; **47**:537–545.
11. Bathe KJ. *Finite Element Procedures*. Prentice-Hall of India Pvt. Ltd: New Delhi, 1997.